PNAS RESEARCH ARTICLE | PHYSICS

Controlling the shape and topology of two-component colloidal membranes

Ayantika Khanra[a,1], Leroy L. Jia[b,1], Noah P. Mitchell[c,d], Andrew Balchunas[e], Robert A. Pelcovits[f], Thomas R. Powers[f,g], Zvonimir Dogic[d,e,h], and Prerna Sharma[a,i,2]

Edited by Tom Lubensky, University of Pennsylvania, Philadelphia, PA; received March 13, 2022; accepted June 13, 2022

Changes in the geometry and topology of self-assembled membranes underlie diverse processes across cellular biology and engineering. Similar to lipid bilayers, monolayer colloidal membranes have in-plane fluid-like dynamics and out-of-plane bending elasticity. Their open edges and micrometer-length scale provide a tractable system to study the equilibrium energetics and dynamic pathways of membrane assembly and reconfiguration. Here, we find that doping colloidal membranes with short miscible rods transforms disk-shaped membranes into saddle-shaped surfaces with complex edge structures. The saddle-shaped membranes are well approximated by Enneper's minimal surfaces. Theoretical modeling demonstrates that their formation is driven by increasing the positive Gaussian modulus, which in turn, is controlled by the fraction of short rods. Further coalescence of saddle-shaped surfaces leads to diverse topologically distinct structures, including shapes similar to catenoids, trinoids, fournoids, and higher-order structures. At long timescales, we observe the formation of a system-spanning, sponge-like phase. The unique features of colloidal membranes reveal the topological transformations that accompany coalescence pathways in real time. We enhance the functionality of these membranes by making their shape responsive to external stimuli. Our results demonstrate a pathway toward control of thin elastic sheets' shape and topology—a pathway driven by the emergent elasticity induced by compositional heterogeneity.

membranes | topological shape transitions | minimal surfaces

Significance

Three-dimensional shaping of thin sheets and membranes is a ubiquitous feature of materials science and underlies diverse biological processes, ranging from large-scale morphogenesis to molecular drug delivery. It is also a familiar everyday phenomenon, as illustrated by the formation of soap bubbles. We demonstrate how flat disk–shaped colloidal membranes transform into saddle-like surfaces. As membranes coalesce, the saddle-shaped surfaces form catenoid-like structures and other architectures of increasing complexity and topological genus. The unique features of our experiments reveal the three-dimensional details of the pathway by which membranes undergo topological shape changes in real time. Our results demonstrate the topological shaping of membrane-like materials through control of their elasticity and Gaussian curvature modulus.

Thin sheets can assume diverse geometrical and topological shapes and structures, which permeate the natural world across length scales. At the cellular level, nanometer-thick fluid-like lipid membranes can seamlessly transition between distinct topological structures, a unique feature that is essential for endo- and exocytosis and viral infection as well as transport of nutrients and signaling molecules (1–11). At organismal scales, micrometer-thin cellular sheets can transform into complex tubular, coiled, and branched structures that underlie the morphogenesis of flowers, visceral organs, and the nervous system (12–17). Designing responsive synthetic materials that can assume the above-described three-dimensional (3D) shapes and topologies observed in biology remains a challenge. So far, work has primarily focused on macroscale stimuli-responsive solid-like elastic sheets that have a finite in-plane shear modulus (18–21). Such materials allow one to engineer lateral stress patterns that yield targeted 3D architectures. However, solid elastic sheets cannot easily fuse into nontrivial topologies. In comparison, nanometer-sized fluid lipid bilayers readily transform between various topologically complex surfaces, but these transitions occur on timescales and length scales that preclude real-time observation. The limitations of both the nanoscale fluid bilayers and the macroscale solid elastic sheets reveal a need for an experimental platform to study formation of topologically complex surfaces.

Motivated by such considerations, we study colloidal membranes, which are micrometer-thick fluid-like monolayers of aligned rod-like particles. They share many properties with lipid bilayers but at larger length scales and slower timescales (22). Introducing a critical fraction of miscible shorter rods destabilizes the flat state, leading to the formation of diverse geometrically and topologically complex surfaces. The length scale of the colloidal membranes enables visualization of 3D pathways by which open flat sheets transform into topologically nontrivial structures. A continuum model describes the membrane shape transitions by balancing the edge energy, which favors flat disk–shaped membranes, with the Gaussian curvature modulus, which favors saddle-shaped structures.

Results

Assembly of Colloidal Membranes. Colloidal membranes are one-rod-length-thick fluid monolayers composed of aligned rods that self-assemble in the presence of depleting

Author contributions: A.K., R.A.P., T.R.P., Z.D., and P.S. designed research; A.K., L.L.J., N.P.M., A.B., R.A.P., T.R.P., Z.D., and P.S. performed research; A.K., L.L.J., N.P.M., and T.R.P. analyzed data; and A.K., L.L.J., N.P.M., R.A.P., T.R.P., Z.D., and P.S. wrote the paper.

The authors declare no competing interest.

This article is a PNAS Direct Submission.

[1]A.K. and L.L.J. contributed equally to this work.

[2]To whom correspondence may be addressed. Email: prerna@iisc.ac.in.

This article contains supporting information online at https://www.pnas.org/lookup/suppl/doi:10.1073/pnas.2204453119/-/DCSupplemental.

Published August 1, 2022.

polymers (22–24). They form by a robust assembly pathway that does not require chemical heterogeneity, such as an amphiphilic nature of the building blocks, but rather, relies on the anisotropy of the building blocks. Entropic depletion interactions favor alignment of the rods along their long axes, which minimizes volume excluded to the polymer coils (25). The attraction strength is determined both by the length of the rods and by the concentration of the depleting polymer. Over an intermediate range of depletant concentrations, such tunable attractions assemble membrane-like materials, in which there is a complete phase separation between the rod-rich membrane and a polymer suspension that envelops the membrane. The density of the rods within a membrane is determined by the osmotic pressure that is exerted by the immiscible polymers. Similar to lipid bilayers, the out-of-plane deformations of colloidal membranes are described by the Helfrich Hamiltonian (26–28). However, unlike lipid bilayers that assemble into edgeless vesicles, colloidal membranes usually assume flat two-dimensional (2D) disk-like shapes. Furthermore, being assembled from 1-μm-long particles, colloidal membranes allow for visualization of various in-plane structures and dynamical pathways that are not easily studied with nanometer-sized lipid bilayers (29–33).

Short Rods Destabilize Flat Colloidal Membranes. We studied binary colloidal membranes assembled from two chiral filamentous viruses with the same handedness, 1,200-nm-long M13KO7 and 880-nm-long M13-wt (34–36). In the presence of the nonadsorbing polymer dextran, both virus types coassembled into 2D colloidal membranes. We first changed the number fraction of short rods, n_{short}, within the membrane while keeping the dextran concentration fixed. The common chirality of the rods increased the miscibility of the two species when compared with rods of opposite chirality (31, 37). At low number fractions of short M13-wt rods ($n_{\text{short}} < 0.15$), we observed assembly of flat colloidal membranes. Labeling both rod types revealed uniformly mixed membranes (Fig. 1 *A*, Top, *B*, Top, *and C*, *Top*). At intermediate volume fractions ($0.2 < n_{\text{short}} < 0.35$), the membranes assumed 3D saddle-like surfaces with negative Gaussian curvature (Fig. 1 *A*, *Middle*, *B*, *Middle*, *and C*, *Middle*). Labeling both virus types revealed that saddle membranes remained uniformly mixed for $n_{\text{short}} < 0.25$. Beyond this fraction, we observed that short rods started phase separating at the membrane's edge, but the interior remained uniformly mixed. Increasing the number fraction of short rods even further ($n_{\text{short}} > 0.35$) yielded another transition from saddle surfaces back to flat membranes. This was accompanied by an in-plane phase separation into two phases that were enriched in the long and short rods, respectively (Fig. 1 *A*, *Bottom*, *B*, *Bottom*, *and C*, *Bottom*).

We mapped the phase diagram as a function of n_{short} and dextran concentrations (Fig. 1*D*). Liquid crystalline tactoids and disordered smectic-like stacks formed at low and high dextran concentrations, respectively (38). Colloidal membranes formed at intermediate dextran concentrations (22). For a fixed intermediate dextran concentration, we found that increasing the fraction of short rods first led to flat and miscible membranes, then led to saddle-shaped miscible membranes, and finally, led to phase-separated flat membranes. At the transition points, flat and saddle-shaped membranes coexisted. Notably, the saddle-shaped membranes existed in a regime of binary colloidal membranes where the length difference between the two rods was not too pronounced and the rods had the same chirality. Both effects enhanced the miscibility of the rods, generating spatially mixed membranes. This is in contrast to previous studies, which explored the strong phase separation regime of colloidal membranes composed of rods with opposite chirality and/or larger length differences (31–33, 37, 39).

Next, we studied the coalescence kinetics of saddle-shaped membranes. Observing the sample over time elucidates how increasing the membrane area affects its 3D shape. Immediately upon preparation, all rods condensed into small colloidal membranes, with lateral size of a few micrometers. Over time, their size increased as the membranes laterally coalesced with each other. Initially, the samples contained colloidal membranes that were mostly saddle shaped (Fig. 2 *A*–*E*). These saddle-like surfaces can be classified according to their order, which characterizes the number of minima and maxima encountered as one moves along the membrane perimeter. Intriguingly, the saddle-shaped membranes exhibit asymmetric distortions along their perimeter, which might be due to the chiral nature of the constituent rods. Even for flat membranes, chirality induces asymmetric rippled

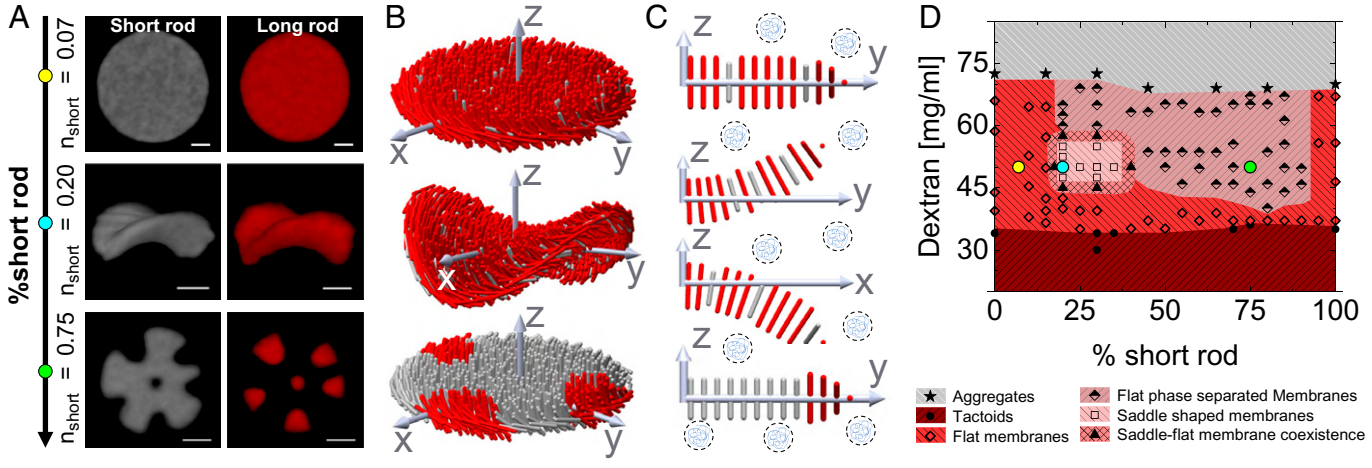

Fig. 1. Phase diagram of binary colloidal membranes. (*A*) Two-component colloidal membranes composed of long (red) and short (gray) rods. Increasing the number fraction of short rods, n_{short}, causes uniformly mixed flat membranes to transform into saddle shapes. At higher n_{short}, phase separation between the two types of rods occurs, and the membranes revert to flat shapes. Dextran concentration is 50 mg/mL. (Scale bars, 2 μm.) (*B* and *C*) Schematics of the rod positions and orientations within membranes at different n_{short}. (*D*) Phase diagram of long and short rod mixtures. Disordered aggregates form above ∼68 mg/mL dextran concentration (filled stars) and tactoids form below ∼35 mg/mL dextran concentration (filled circles). At intermediate dextran concentrations, the following types of colloidal membranes are observed: flat and phase separated (half-filled diamonds), flat and uniformly mixed (open diamonds), and membranes with negative Gaussian curvatures (open squares). Filled triangles correspond to the coexistence of flat membranes and saddles. Yellow-, cyan-, and green-filled circles correspond to the assembly conditions of the membranes shown in *A*.

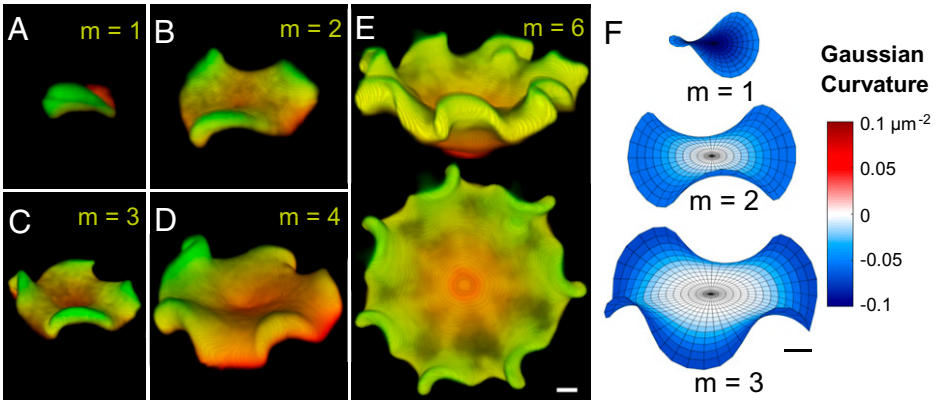

Fig. 2. Saddle-shaped colloidal membranes mimic Enneper surfaces. (*A–D*) Confocal images of saddle-shaped colloidal membranes with increasing order number $m = 1$, 2, 3, and 4. (*E*) 3D-rendered images of deconvolved wide-field z stacks of an $m = 6$-order saddle surface. Dextran concentration is 50 mg/mL, and $n_{short} = 0.2$. (Scale bar, 2 μm.) (*F*) Enneper surfaces of orders $m = 1$, 2, and 3. Color indicates the Gaussian curvature. The area increases with the surface order m, a trend observed in the experiments. (Scale bar, 2 μm.)

edge fluctuations (28). We observed up to sixth-order saddle membranes (Fig. 2*E* and *SI Appendix*, Fig. S1).

Saddle-Shaped Membranes Are Enneper-Like Minimal Surfaces. Saddle-shaped colloidal membranes (Fig. 3*A*) have negative Gaussian curvature and small mean curvature. To quantify their shape, we extracted the membrane midplane from 3D confocal images and computed the spatial maps of both their Gaussian curvature K and mean curvature H (*SI Appendix*, *SI Text*). The median value of the Gaussian curvature was negative ($\langle K \rangle = -0.063\ \mu m^{-2}$), while the median mean curvature was much smaller when compared with the square root of the Gaussian curvature ($\langle H \rangle = 0.010\ \mu m^{-1} \ll \sqrt{|\langle K \rangle|}$). Both curvatures had small-scale heterogeneity due to measurement noise (Fig. 3 *B* and *C*). These results suggest that saddle membranes are well approximated by minimal surfaces.

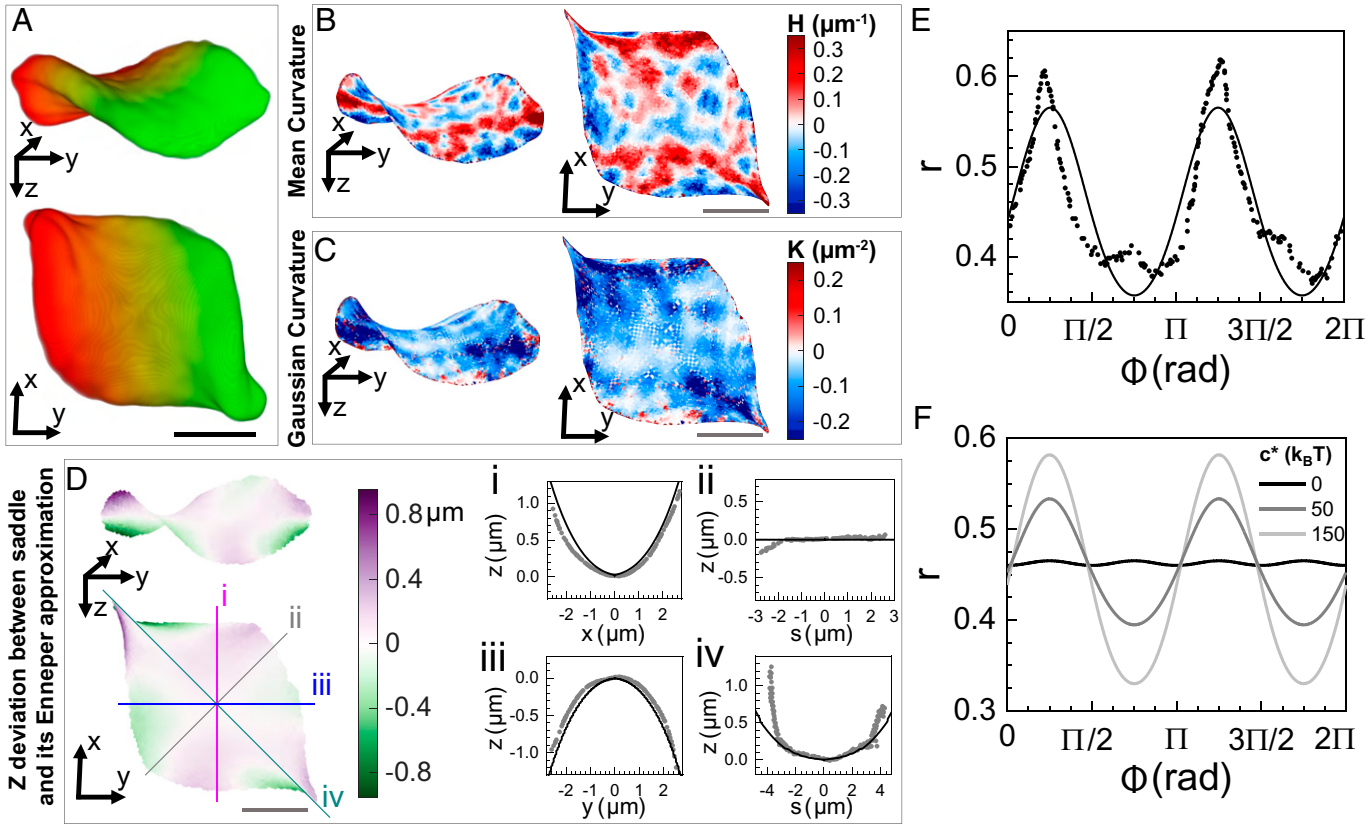

Fig. 3. Saddle-shaped membranes are nearly Enneper minimal surfaces. (*A*) Top and side views of a saddle membrane, rendered from confocal z stacks. (*B* and *C*) Top and side views of the midsurface of the saddle membrane. Color indicates the local mean and Gaussian curvature in *B* and *C*, respectively. The membranes have predominantly negative Gaussian curvature and nearly zero mean curvature. (*D*) Top and side view comparison between an experimental midsurface and the numerical model. Color indicates deviation between the best-fit Enneper surface (size parameter, $R = 6.47$ μm) and the membrane along the z axis. *D*, *i–iv* show height profiles of the midsurface (gray dots) and the best-fit Enneper surface (black curves). (Scale bars, 2 μm.) (*E*) The r–ϕ parameterization of the edge of the saddle shown in *B*. Black dots are experimental measurements, and the black curve is a theoretical prediction in which the Gaussian and chirality moduli are set to 1,000 and 100 k_BT, respectively. (*F*) In theoretical predictions, increasing the chirality modulus elongates the saddle in diametrically opposite directions, resulting in two peaks in the r–ϕ plot of the saddle's edge.

Inspection of different minimal surface families revealed a resemblance between saddle membranes and Enneper minimal surfaces (Fig. 2*F*) (40). The Enneper minimal surfaces have the parameterization

$$\frac{x}{R} = r\cos\phi - \frac{r^{2m+1}}{2m+1}\cos[(2m+1)\phi] \quad [1]$$

$$\frac{y}{R} = r\sin\phi + \frac{r^{2m+1}}{2m+1}\sin[(2m+1)\phi] \quad [2]$$

$$\frac{z}{R} = \frac{2r^{m+1}}{m+1}\cos[(m+1)\phi], \quad [3]$$

where r is a dimensionless radial coordinate, ϕ is the angular coordinate, $m \geq 1$ is the order, and R is a positive parameter (40). Note that r ranges from zero to $r_{\mathrm{edge}}(\phi)$, where the function $r_{\mathrm{edge}}(\phi)$ describes the shape of the edge. The edge of the experimental surface did not extend the same distance in all directions. For instance, the surface extended much farther along one diagonal when compared with the other one (Fig. 3 *D*, lines *ii* and *iv*). We take the surface area to be $A = \pi R_0^2$. When R is much greater than R_0, the saddle is gently curved and has a disk-like shape. As R decreases toward R_0, the surface curvature increases, and the surface self-intersects if R becomes sufficiently small. By adjusting the R parameter, we found Enneper surfaces that well approximate the shapes of representative saddle membranes, with some discrepancies being observed close to the membrane's edge (Fig. 3*D*). The fits for the higher-order experimental surfaces were also less accurate due to the appearance of a central bulge and the chiral structure of the edge (Fig. 2 *E*, *Upper*).

Theoretically Determining the Shape of the Membrane Edge. We introduce a theoretical model to determine the shape of the membrane edge, which is given by $r_{\mathrm{edge}}(\phi)$. Since the tilt of the rods within a saddle membrane is small everywhere except near the edge, we use a continuum model with an effective edge energy to account for the liquid crystalline degrees of freedom close to the edge. This model accounts for the membrane composition implicitly through the assumption that changing the fraction of long and short rods primarily affects the values of the elastic moduli.

The conformation of a colloidal membrane is described by an energy that accounts for a resistance to bending (26, 41), a fixed area, a free edge with an edge tension, a resistance to edge bending, and a preference for a twist due to the chiral constituents (28, 42):

$$E = \frac{\kappa}{2}\int \mathrm{d}A(2H)^2 + \bar{\kappa}\int \mathrm{d}AK + \mu\int \mathrm{d}A + \gamma\int \mathrm{d}l + \frac{B}{2}\int \mathrm{d}lk^2 + \frac{B'}{2}\int \mathrm{d}l(\tau_{\mathrm{g}} - \tau_{\mathrm{g}}^*)^2, \quad [4]$$

where κ is the bending modulus, $\bar{\kappa}$ is the Gaussian curvature modulus, $\mathrm{d}A$ is the element of area of the membrane midsurface, μ is a Lagrange multiplier enforcing area conservation, γ is the edge tension, $\mathrm{d}l$ is the element of arclength of the edge, k is the curvature of the edge, τ_{g} is the geodesic torsion (43), τ_{g}^* is the spontaneous geodesic torsion (proportional to the desired rate of twist), and B and B' are the elastic moduli associated with the edge. It is convenient to work in terms of the chirality modulus $c^* = -B'\tau_{\mathrm{g}}^*$.

We can independently estimate the magnitude of the phenomenological parameters in Eq. **4**. Measurements of the fluctuations of the edge of a disk-like membrane ($n_{\mathrm{short}} = 0.1$) reveal that $B \approx 150\ k_B T$ μm and $\gamma_{\mathrm{eff}} \approx 620\ k_B T/\mu\mathrm{m}$ (*SI Appendix*, Fig. S2) (29). There is a chiral contribution to the line tension $\gamma_{\mathrm{c}} = (c^*)^2/(2B')$, so that the effective total line tension is $\gamma_{\mathrm{eff}} = \gamma + \gamma_{\mathrm{c}}$ (29). We also assume that $B' = B$. Furthermore, colloidal membranes' area compressibility implies a large value of the bending modulus, $\kappa \approx 15,000\ k_B T$ (24). Membranes with a positive Gaussian modulus decrease their energy by adopting negative Gaussian curvature, and the Gaussian moduli of both single-component fd-wt and mixed fd-wt/fd-Y21M membranes have a magnitude of $\sim 200\ k_B T$ and are positive (27, 28). Thus, we expect $\kappa \gg \bar{\kappa}$, which provides an additional rationale for modeling saddles as Enneper minimal surfaces (Fig. 2*F*).

Assuming that the nonflat membranes are described by mth-order Enneper surfaces, we determine the boundary contour by solving the in-plane force balance equation for the edge, $r_{\mathrm{edge}}(\phi)$, subject to the constraints of the fixed area and periodicity in ϕ (*SI Appendix*, Eq. **3**). The minimal surface assumption ($\bar{\kappa} \ll \kappa$) implies that the other equilibrium conditions for out-of-plane force balance (*SI Appendix*, Eq. **2**) and moment balance (*SI Appendix*, Eq. **4**) at the membrane's edge are trivially satisfied since the terms proportional to κH or $\kappa\nabla H$ can take whatever values are necessary to satisfy these equations when $\kappa \to \infty$ and $H \to 0$.

The numerical model correctly captures the $(m+1)$-fold dihedral symmetry of the Enneper surface. Generically, we find that a one-mode approximation $r_{\mathrm{edge}}(\phi) \approx r_0 + r_1\cos[(m+1)(\phi - \phi_0)]$, for constants r_0, r_1, and ϕ_0, is sufficient to describe the solutions to Eq. **3** (*SI Appendix*). Notably, the amplitude r_1 depends weakly on $\bar{\kappa}$ but strongly on c^* (Fig. 3*F*). However, increasing c^* or $\bar{\kappa}$ decreases the value of R that minimizes the energy E since these changes cause the surface to prefer additional curvature.

We determine $\bar{\kappa}$ and c^* by fitting the edge profiles of the saddle surfaces. During the fitting process, γ and B are fixed at the values mentioned above, and R is fixed at the value obtained from fits of the midsurface. For the saddle shown in Fig. 3 *A*–*D* ($R = 6.47$ μm), $\bar{\kappa} \approx 1{,}000\ k_B T$, and $c^* \approx 100\ k_B T$ (Fig. 3*E*). Fitting of the edge profiles of other saddles of various orders yields similar results. We note that the magnitude of the chiral modulus is comparable with previous estimates (28, 42), while $\bar{\kappa}$ is nearly an order of magnitude greater than the value for single-component membranes. Also, recall that the Gauss–Bonnet theorem shows that the Gaussian curvature energy is effectively an edge energy, despite the fact that it is written as an integral over the entire surface in Eq. **4**.

Continuum Model Estimates the Stability of Saddle-Shaped Membranes. Using our continuum model, we estimate the stability of Enneper-like surfaces. Our focus is on the transition between flat disks and Enneper surfaces and between Enneper surfaces of different orders. We use the above-described parameter values to minimize Eq. **4**. For a given area, we calculate the energies of the 11 lowest-order saddles using the numerical procedure outlined above as functions of R, which is determined numerically through minimization. While driving R to zero almost always results in an absolute minimum, local minima where $\partial E/\partial R = 0$ and $\partial^2 E/\partial R^2 > 0$ also occur for certain parameter combinations. Fig. 4*A* shows a range of areas $R_0 = \sqrt{A/\pi}$ and the values of m for which Enneper surfaces have lower energy than a flat disk of equivalent area. The effects of a larger or smaller $\bar{\kappa}$ were also explored (*SI Appendix*, *SI Text* and Fig. S3).

For the smallest membrane sizes, only the lowest-order saddles are stable since higher-order Enneper surfaces have more Gaussian curvature. As R_0 increases, the theoretical range of allowable saddles broadens, with the energy-minimizing saddle

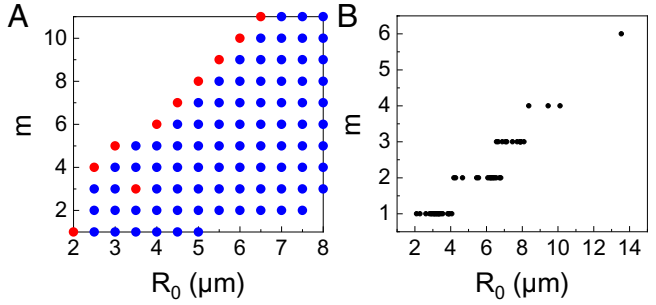

Fig. 4. Saddle order increases with an increase in surface area. (*A*) The values of m for which there exist Enneper surfaces that are stable and lower energy than the disk of radius $R_0 = \sqrt{A/\pi}$. Blue dots indicate the existence of such a saddle; red dots indicate the stable saddle of lowest energy. For most areas, this happens at the maximum allowable m. Energies were computed for a membrane with $\gamma = 622\ k_BT/\mu m$, $B = B' = 155\ k_BT\ \mu m$, $c^* = 100\ k_BT$, and $\bar{\kappa} = 1{,}000\ k_BT$. As area increases, the lower-order saddles become less energetically favorable compared with the disk, while the higher-order saddles become more energetically favorable. Saddles of order up to and including $m = 11$ were compared in this plot. (*B*) Ranges of experimentally observed saddle sizes and corresponding saddle orders. Membrane z stacks were taken from a combination of confocal and deconvolution microscopy; the smallest membranes ($R_0 < 2\ \mu m$) were not processed. While the theory tends to overestimate m, the general trend of m linearly increasing as R_0 increases is clearly visible.

having the highest allowable m. There is one exception at $R_0 = 3.5\ \mu m$, which is possibly due to the existence of multiple-solution branches (*SI Appendix*). At the largest areas, the lowest-order saddles are no longer favorable compared with the disk since the edge cost at small m is larger than the Gaussian curvature energy gained by curving it into a saddle. None of the local minima exhibit self-intersection. The emergence of energy-minimizing saddles as area is increased appears to be a first-order transition.

This phase diagram is in qualitative agreement with the experimental result that low-order saddles are observed for small area membranes and that increasing the area leads to higher-order saddles, with a dependence that appears almost linear (Fig. 4*B*). The theory tends to overestimate the order of saddles at higher areas. It is reasonable to expect our simple theory to become less accurate at higher areas since our theory does not account for the sag that occurs for larger membranes or for the interaction of the sagging region with the coverslip.

Topological Transitions. Flat disk–like membranes grow in size through lateral coalescence events (44). In comparison, saddle-like surfaces exhibit two distinct coalescence pathways. Lateral coalescence events lead to Enneper-like surfaces of greater area, sometimes of the same order and sometimes of a higher order. However, we also observed a distinct coalescence pathway that changes the topology of the membrane. A 2D section of two saddle-shaped membranes undergoing coalescence via this pathway is not very revealing (Fig. 5*A* and Movie S1). To gain insight, we used the unique features of colloidal membranes that allowed for visualizing the coarsening pathways with unprecedented detail. First, micrometer-sized colloidal membranes in combination with fast z scanning and 3D deconvolution microscopy enabled visualization of complex 3D surfaces. Second, the large size of colloidal membranes slowed the coalescence dynamics, thus enabling real-time visualization. Leveraging these features revealed that the two coalescing saddle-shaped surfaces transition into topologically distinct catenoid-like shapes (Fig. 5*B* and Movie S2) with nonzero mean curvature (*SI Appendix*, Fig. S5).

Multiple observations suggest that the assembly pathway for the catenoid-like shape is robust. Two saddle surfaces approached each other at an almost right angle and fused at a specific location away from the edge of either membrane. Therefore, the point of initial contact was in the interior of both membranes where the rods are normal to the surface. Following this event, a fusion pore nucleated in the vicinity of the initial contact point. This pore grew to a well-defined size along with the continuous transformation of the object into a catenoid-like shape. In comparison, the edge-to-edge lateral coalescence of two saddle-shaped membranes yielded larger or higher-order saddles (Movies S1 and S3).

Catenoid-like membranes were intermediate structures. In the next step, such shapes merged with a saddle surface to transition into a topologically distinct surface with three openings (Fig. 6 *A*, *Middle*). These were similar to three-noids, which are minimal

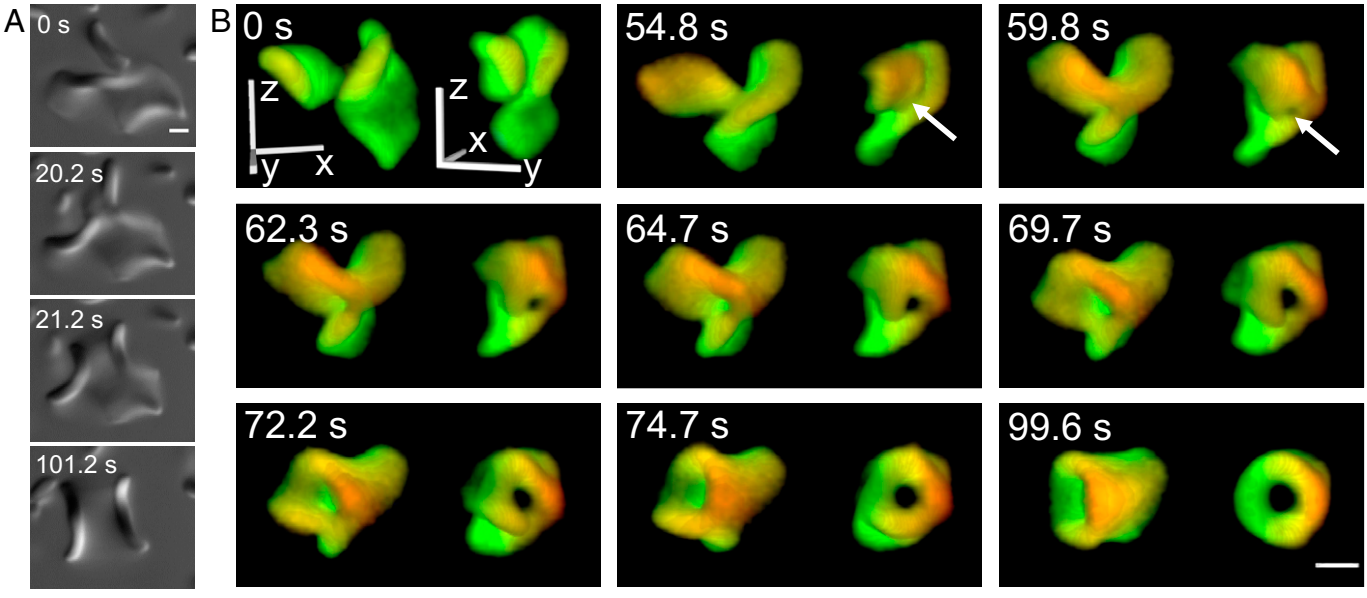

Fig. 5. Saddle-shaped surfaces coalesce to form catenoid-like membranes. (*A*) Coalescence of two saddle-shaped membranes, observed with differential interference contrast (DIC) microscopy. (*B*) Time-lapse 3D false-colored images of the intermediate steps of the coalescence process. These images are obtained by deconvolving z stacks captured using fluorescence microscopy of saddles containing fluorescently labeled long rods. The event is shown from two orientations, with coordinate axes specified in *Top Left*. Dextran concentration is 50 mg/mL; $n_{short} = 0.2$. The arrows indicate the singularity associated with the formation of a hole. (Scale bars, 2 μm.)

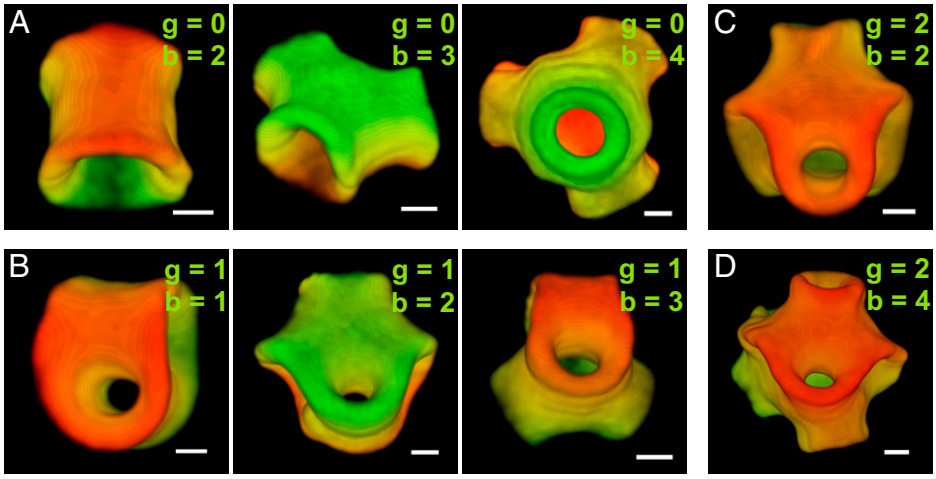

Fig. 6. Topologically complex membranes of a different genus. The topology is characterized by the genus g and the number of boundaries (edges) b. (*A*) A catenoid-like membrane and its derivatives, which have the topology of a three-noid and a four-noid. (*B*) Membrane shapes with the topology of a saddle with a handle, a catenoid with a handle, and a three-noid with a handle. (*C* and *D*) Two complex surfaces of a genus of two with $b = 2$ and 4, respectively. Dextran concentration is 50 mg/mL; $n_{short} = 0.2$. (Scale bars, 2 μm.)

surfaces having saddle-splay curvature in the form of a catenoid with three openings. The transition from the catenoid-like shape to the shape with three openings involved nucleation and growth of a fusion pore away from the catenoid edge (Movie S4). Subsequent coalescence events generated surfaces of increasing complexity (Fig. 6 and Movie S5). Besides catenoid-like and three-noid-like shapes, we also observed membranes with the topology of four-noids (Fig. 6*A*). Well-equilibrated samples showed larger and more complex structures with many handles (Fig. 6 *B*–*D*). The size of the structures and their topological complexity were limited by the slowing coalescence kinetics. Eventually, Brownian motion of large assemblages slowed down, which reduced further coalescence events. To overcome this limitation, we tilted the sample. Subsequently, intermediate structures slowly sedimented, accumulating at the bottom. There, they came in close contact, coalescing further. Such conditions generated macroscale structures, which resembled sponge phases of amphiphilic molecules (Fig. 7*A* and *SI Appendix*, Fig. S4). Confocal microscopy revealed the internal structures of such large-scale assemblages. Regions with quasiperiodicity were found, wherein three-way open tunnels in each layer rotate by 60° with respect to the consecutive layer (Fig. 7*B* and Movie S6).

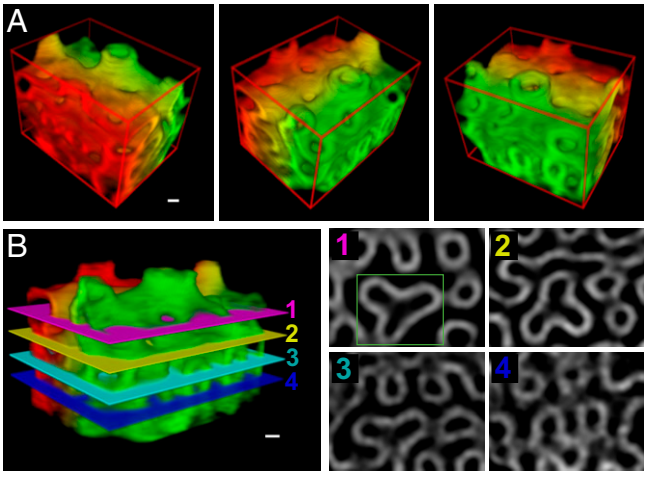

Fig. 7. Colloidal sponge-like phases. (*A*) Three different 3D false-colored views of a network-like structure with a genus of 41. (*B*) Representative planes within this structure are marked as 1, 2, 3, and 4. Gray-scale images are 2D cross-sections of the planes. Rod concentration is 2 mg/mL, dextran concentration is 50 mg/mL, and $n_{short} = 0.2$. (Scale bars, 2 μm.)

We characterized the topology of the above-described structures using the number of edges or boundaries b and the genus g of the membrane midsurface. The genus of the midsurface is equal to the number of doughnut holes in that surface or equivalently, the minimal number of closed cuts that leave the remaining surface in one piece. Thus, the saddle has one boundary and a genus of zero (Fig. 3*A*). The catenoid-like membrane also has a genus of zero but two boundaries; adding edges to get the analogs of the three- and four-noid leaves g unchanged but increases b (Fig. 6*A*). The membranes in Fig. 6*B* all have a genus of one, and they have topologies of a saddle with a handle (Fig. 6 *B*, *Left*), a catenoid with a handle (Fig. 6 *B*, *Center*), and a trinoid with a handle (Fig. 6 *B*, *Right*), respectively. Fig. 6 *C* and *D* shows structures with higher genus and more boundaries. The sample spanning structures are more meaningfully characterized by a genus density of one hole every 390 μm^3, instead of the absolute value of genus.

While genus characterizes the global topology of the self-assembled shapes, spatial maps of mean and Gaussian curvature serve as metrics of local topology. All assemblages had negative Gaussian curvature over large parts of their surface (Fig. 3*C* and *SI Appendix*, Fig. S5). Except for the lowest-order saddles, all other complex membranes had finite mean curvature whose spatial variation was connected to the topology (*SI Appendix*, Fig. S5). For example, mean curvature varied along the symmetry axis of the catenoid-like membrane (*SI Appendix*, Fig. S5*D*). The saddle with a handle had opposite mean curvature in the two tunnels (*SI Appendix*, Fig. S5*G*). The more complex assemblages, such as three- and four-noid, had predominantly negative Gaussian curvature throughout, except for a well-defined region near the midsection (*SI Appendix*, Fig. S5 *E* and *F*).

Microscopic Membrane Structure. Next, we investigate how membrane curvature couples to the orientation of the constituent rods with respect to the surface normal (45). We imaged catenoid-like membranes that were sparsely doped with fluorescently labeled viruses (Fig. 8 *C* and *D* and Movie S7). Similar to flat membranes (29, 30), rods twisted at the exposed edges of the catenoid-like membranes. In comparison, close to the catenoid midsection the rods point along the surface normal, generating a radial arrangement (Fig. 8*D*). For our analysis, the catenoid symmetry axis points along the z axis, while the circular midsection lies in the x–y plane (Fig. 8*D*). We quantified the edge-induced twisting by plotting the angular deviation of the

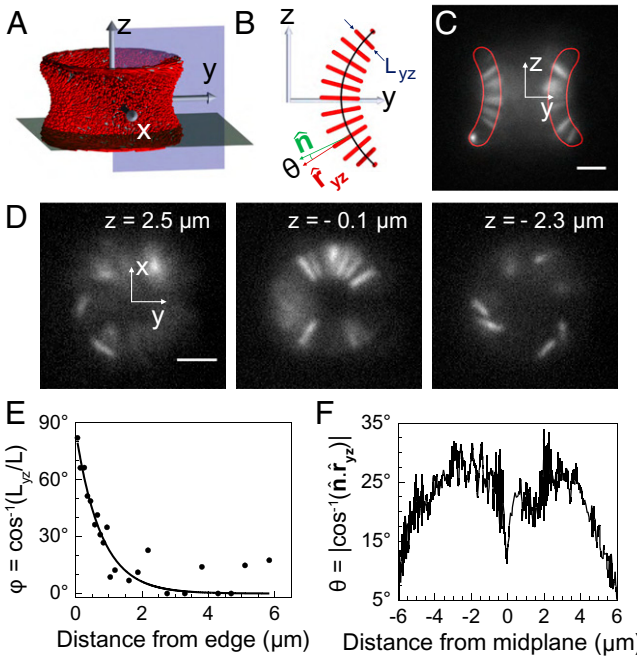

Fig. 8. Orientation of rods in a catenoid-like membrane. (*A*) Schematic showing *x*–*y* (gray) and *y*–*z* (violet) planes. (*B*) Schematic depicting variables that characterize rod orientation. (*C*) Fluorescence images of individual long rods imaged in the $x = 0$ plane, with the virus-solvent interface outline shown in red. (*D*) Individual long rods imaged at *x*–*y* planes corresponding to different *z* values, showing a twist in rod orientation. (*E*) Twist angle φ, the angle by which the rods tilt away from the *y*–*z* plane, as a function of the distance from the edge is shown. *L* is the length of the long rods. An exponential fit (black line) to this plot gives a twist penetration depth of 700 nm. (*F*) Variation of θ, the absolute value of the angle between the *y*–*z* plane projection of rods, $\hat{r}_{yz}$, and the surface normal of membrane, $\hat{n}$, with the distance from midplane ($z = 0$). The angle θ is zero for flat membranes, but for catenoid-like membranes, we find a significant deviation from zero. Dextran concentration is 50 mg/mL, and $n_{short} = 0.2$. (Scale bars, 2 μm.)

rod axis with respect to the y–z plane (Fig. 8*B*), also known as the twist angle. Twist angle decayed exponentially from ∼90° to zero with distance from the edge, with a decay constant of 700 nm (Fig. 8*E*), comparable with the twist penetration depth in flat membranes (30). An anomalous behavior is seen when rod orientation in a catenoid-like membrane is observed in the y–z midplane; the projection of rods deviates up to 25° from the local surface normal (Fig. 8*F*). This deviation of the rod axis from the local surface normal leads to an additional free energy cost, which might be reduced by the bump that appears in the midsection of large catenoid-like membranes (*SI Appendix*, Fig. S6*A*). Rod orientation in saddles of order $m = 1$ is nearly along the local surface normal everywhere except near the edges (*SI Appendix*, Fig. S7).

In principle, short rods could preferentially reside next to the inner or outer membrane surface or close to the membrane midplane (37). By labeling both rods types, we determined the center of mass of both short rods and long rods (*SI Appendix*, Fig. S8). Such efforts demonstrate that the center of mass of short rods is preferentially located at the membrane midplane.

Stimuli-Induced Membrane Folding. The phase diagram shows that the disk to saddle transition occurs with increasing dextran concentration or equivalently, the osmotic pressure (Fig. 1*D*). Instead of dextran, we assembled membranes with poly(ethylene glycol) (PEG), a polymer whose osmotic pressure exhibits significant temperature dependence (46). The saddle to disk transition could be induced by changing the sample temperature. We assembled saddle-shaped membranes at room temperature. Elevating the sample temperature to 60 °C in situ decreased the osmotic pressure of the enveloping polymer and concentration of the rods within the membrane. In response, the saddle membrane transformed into a flat disk. The saddle to disk transition was reversible (Movie S8). On decreasing the temperature, curved regions nucleated near the edge of the flat membrane, and eventually, a saddle formed (Fig. 9*A* and Movie S9).

Topology influenced the stability of curved surfaces. At 60 °C, most saddle surfaces transformed into flat disk–shaped membranes. In comparison, the catenoid-like membranes showed almost no shape change, except for a slight increase in the neck radius. Increasing the temperature further to ∼ 70 °C destabilized these membranes; they transitioned into disks by a specific kinetic pathway. In the first step, one of the two exposed edges started decreasing in radius and finally, closed. Subsequently, the curved surface transformed into a flat membrane (Fig. 9*B*). The transition from the catenoid-like shape to the disk was irreversible.

Estimating Gaussian Curvature Modulus. Stability of saddles suggested that the Gaussian modulus of two-component membranes is $\bar{\kappa} \approx 1{,}000\ k_B T$. A simple model explains this finding. We first note that several independent measurements suggest that single-component colloidal membranes have a $\bar{\kappa} \approx 200\ k_B T$ (27, 28, 42). This value can be explained by the increase in the volume available to the depleting polymers when the membrane assumes a saddle-like negative Gaussian curvature, which leads to a positive contribution $\bar{\kappa}_p$ to the Gaussian curvature modulus, $\bar{\kappa}_p = (D + d)^3 n k_B T/12$, where D is the thickness of the colloidal membrane, d is the diameter of the depleting polymer, and n is the number density of the polymers (27). The membrane itself contributes a negative contribution $\bar{\kappa}_m$, which is given by

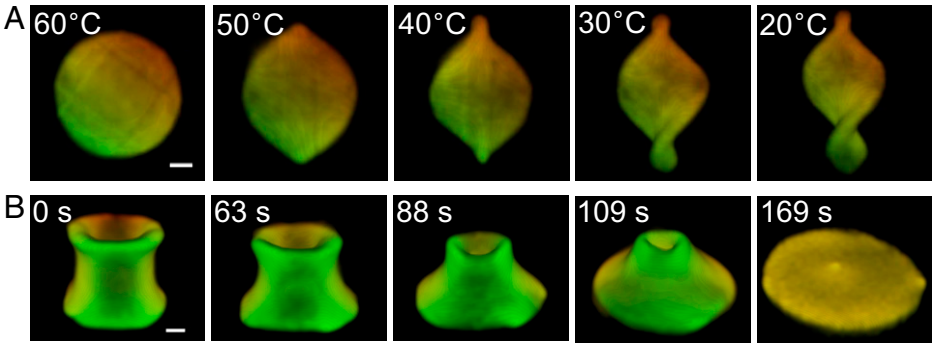

Fig. 9. Stimuli-responsive colloidal membranes change geometry and topology. (*A*) A flat membrane transforms into a twisted saddle or a helicoid upon decreasing temperature, which increases the strength of the depletion attraction. (*B*) A catenoid-like shape transforms into a flat membrane after elevating temperature to 70 °C. Time-lapse images show deconvolved *z* stacks that were 3D rendered in false color. The samples were self-assembled at room temperature with $n_{short} = 0.23$ and 15.6 mg/mL of PEG 35K as depletant dissolved in 175 mM NaCl and 20 mM Tris, pH 8 buffer. (Scale bars, 2 μm.)

the second moment of the in-plane lateral stress σ of the flat state, $\bar{\kappa}_{\rm m} = \int \sigma z^2 {\rm d}z$, where z measures distance across the membrane thickness, measured from the midplane (47, 48).

For membranes containing a small number fraction α of short rods of length $D_{\rm s}$ among long rods of length $D_{\rm l}$, we estimate the second moment of the in-plane stress as

$$\int \sigma z^2 {\rm d}z = \alpha \int_{-D_{\rm s}/2}^{D_{\rm s}/2} \sigma_{\rm s} z^2 {\rm d}z + (1-\alpha) \int_{-D_{\rm l}/2}^{D_{\rm l}/2} \sigma_{\rm l} z^2 {\rm d}z, \quad [5]$$

where $\sigma_{\rm s,l} = -nk_{\rm B}T(D_{\rm s,l} + d)/D_{\rm s,l}$ is the compressive stress due to the osmotic forces of the polymers that arises in a flat membrane composed of short rods only or long rods only.

Assuming at small volume fraction α, the short rods do not affect the polymeric contribution $\bar{\kappa}_{\rm p}$ and that $D_{\rm s,l} \gg d$, we find that

$$\bar{\kappa} = \bar{\kappa}_{\rm p} + \bar{\kappa}_{\rm m} = \frac{1}{6} nk_{\rm B}TD_{\rm l}^2 d + \frac{\alpha}{12} nk_{\rm B}T(D_{\rm l}^3 - D_{\rm s}^3). \quad [6]$$

The Gaussian curvature modulus $\bar{\kappa}$ increases linearly with the number fraction of short rods at small number fraction because increasing the number of short rods decreases the magnitude of the negative contribution $\bar{\kappa}_{\rm m}$. For dextran polymers with $d = 30$ nm, a molecular weight of 500,000 g/mol, and a concentration of 50 mg/mL, we estimate the Gaussian modulus to be $\bar{\kappa}_{\rm l} \approx 400\, k_{\rm B}T$ for a membrane composed of long rods only and $\bar{\kappa}_{\rm s} \approx 200\, k_{\rm B}T$ for a membrane composed of short rods only. At a short rod fraction of $\alpha = 0.2$, the correction is $\alpha nk_{\rm B}T(D_{\rm l}^3 - D_{\rm s}^3)/12 \approx 1{,}000\, k_{\rm B}T$. We need to mention a caveat in order not to overinterpret our simplified model. Specifically, the validity of applying this formula to membranes composed of heterogeneous molecules, such as lipids, has been called into question (49).

Discussion and Conclusions

We described the diverse 3D shapes observed in two-component miscible colloidal membranes. Increasing the fraction of short rods destabilized flat disk–like membranes, leading to the assembly of saddle-shaped Enneper-like surfaces. These intermediate structures continued coalescing with each other to form topologically more complex structures. The micrometer-length scale of colloidal membranes enabled visualization of the multistep coalescence pathway in real time.

Theoretical analysis suggests that the stability of disk-like membranes is controlled by the Gaussian modulus. Our proposed model is too crude to quantitatively predict the boundaries of the disk to saddle transition, but it suggests the following qualitative explanation. The edge tension favors flat disk–like membranes. At low volume fraction of short rods, the intrinsic Gaussian curvature modulus is not high enough to overcome the desire of the edge tension to keep the membrane flat. Increasing the fraction of short rods favored the formation of saddle surfaces. In the saddle regime, the Gaussian modulus is large and positive; thus, saddle-shaped surfaces decrease the membrane deformation energy, compensating for the excess edge that is associated with the formation of a nonflat surface. This strongly suggests that increasing the fraction of short rods increases the magnitude of the Gaussian modulus. A simple geometrical argument based on excluded volume explains how the fraction of short rods controls the Gaussian curvature modulus. Finally, increasing the fraction of short rods even further induces lateral phase separation. Thus, the Gaussian curvature modulus drops abruptly, and one recovers flat disk–shaped phase-separated membranes. Previous studies have observed different surfaces with negative Gaussian curvature, namely twisted ribbons (29, 42). Those studies used a virus, which had significantly lower edge tension. Extended twisted ribbons have excess edge energy when compared with the compact structures studied here.

Colloidal membranes and conventional lipid bilayers are described by the same continuum energy (26). Thus, besides demonstrating a robust method for shaping colloidal membranes, our results also advance the understanding of all membrane-based materials. The Gaussian modulus is a key physical quantity that governs phenomena involving membrane curvature generation and modulation, such as endocytosis and exocytosis, cell differentiation, and cell motility (50–55). Conventional lipid bilayer vesicles do not permit easy understanding of how the Gaussian modulus affects their morphology, as the Gauss–Bonnet theorem requires that the Gaussian curvature energy integrates to a system-independent constant value (6, 56, 57). Consequently, measurement and control of the Gaussian modulus in lipid bilayers is challenging (58–60). Open edges of colloidal membranes enabled our study of how the Gaussian modulus influences the stability of flat disk–shaped membranes. Our method of tuning the Gaussian modulus by doping membranes with miscible short rods reveals a microscopic mechanism that cells could use for curvature generation and maintenance.

Ranging from simple crystals and liquid crystals to more exotic polymers, glasses, alloys, and diamond-like structures, colloids can form analogs of diverse atomic materials (61–64). Colloidal length scale provides a unique opportunity to visualize the real space structure and dynamics that are inaccessible in atomic materials. The structures we observed at the end stages of the coalescence are reminiscent of finite-sized cubosomes and gyroid-like phases observed in conventional amphiphilic systems (65–68). The colloidal length scale of our system allowed for detailed real-time imaging of the molecular assembly pathways. For example, we have observed how two saddle-shaped surfaces come together to form a topologically distinct catenoid-like structure. Intriguingly, this coalescence proceeds when two surfaces come together at a very specific orientation and is accompanied by the formation of a fusion pore and its subsequent enlargement. A detailed understanding of this robust dynamical pathway warrants future studies.

More broadly, many dynamical processes, such as the breakup of fluid droplets, exhibit shape transformations that are characterized by the appearance of singularities (69, 70). Membrane-based processes, such as infection of membrane-enveloped viruses, also exhibit singularities as they undergo fission and fusion transformations. However, the molecular length scale of lipid bilayers prevents visualizing the dynamics of these singularities. Our experiments at micrometer-length scales reveal that fusion of saddle-shaped membranes into a catenoid-like shape has an intriguing singularity, involving the creation of a fusion pore and its growth.

Finally, our work provides a mechanism for topological shaping of thin elastic membrane-like sheets by controlling their Gaussian modulus. This complements the usual technique of folding sheets through mechanical instabilities induced by in-plane differential swelling/shrinkage or application of external confining forces (20, 21, 71). We foresee that spatial control of the Gaussian modulus of colloidal membranes would lead to an even richer landscape of topologically complex surfaces.

Materials and Methods

M13KO7 and M13-wt viruses were grown using the host *Escherichia coli* strain ER2738 following standard biological protocols (72). Gel electrophoresis revealed that the purified M13-wt virus had a significant amount of end-to-end multimers, which prevents defect-free membrane formation. The multimers were removed using isotropic–nematic phase separation (22). All viruses were suspended in 100 mM NaCl and 20 mM Tris HCl (pH = 8.0) media.

Viruses were labeled with either DyLight 550 or DyLight 488 (Thermo Fisher Scientific) amine reactive dye for the purpose of fluorescence imaging. There are ∼3,600 and ∼2,700 labeling sites on M13KO7 and M13-wt rods, respectively. Ten percent of the sites were labeled for experiments that image the motion and orientation of individual rods. One percent of the sites were labeled for all other experiments.

The number density of viruses in a given suspension was measured with an ultraviolet-visible spectrophotometer (Multiscan GO; Thermo Fisher Scientific). The two kinds of viruses were mixed at the desired stoichiometric ratio, and dextran (500 kDa molecular weight; Sigma-Aldrich) was added. Coverslips were coated with a polyacrylamide brush before sample preparation to prevent membranes from adhering to coverslips. Sample chambers were made from coated coverslips and cleaned slides, using parafilm as a spacer. The suspension was injected into the chamber, and the chamber was sealed with optical glue (Norland).

Samples were observed using an inverted wide-field microscope (Olympus IX83) equipped with a 100 × oil immersion phase and differential interference contrast (DIC) objectives (UPLanFLN-100X/1.30 Oil Ph3, UPLanFLN-100X/1.30 Oil), motorized *z* drive, and CCD (charge-coupled device) and EMCCD (electron multiplying charge-coupled device) cameras (Photometrics CoolSNAP HQ2 and Andor iXon Ultra 888). A Peltier stage (PE120; Linkam) was used to vary sample temperature. Z stacks were captured using this microscope in fluorescence mode, followed by deconvolution to represent the structures in 3D qualitatively. A confocal microscope (Zeiss LSM 880 Airyscan equipped with a Plan Apo 63 × 1.4 numerical aperture oil objective) was used for capturing *z* stacks for quantitative analysis.

Data Availability. All study data are included in the article and/or supporting information.

ACKNOWLEDGMENTS. We thank Megan Kerr for helpful discussions. A.K. and P.S. acknowledge funding support from Science and Engineering Research Board and Department of Science & Technology Grant CRG/2019/000855; N.P.M., A.B., and Z.D. acknowledge primary support from NSF Grant NSF-DMR-1905384; N.P.M. acknowledges support from the Helen Hay Whitney Foundation; and R.A.P. and T.R.P. acknowledge support from NSF Grant NSF CMMI-2020098. We also acknowledge support of NSF Materials Research Science and Engineering Centers Grants DMR-1420382 (to R.A.P., T.R.P., and Z.D.) and DMR-2011846 (to T.R.P. and Z.D.). This research was supported in part by NSF Grant NSF PHY-1748958.

Author affiliations: [a]Department of Physics, Indian Institute of Science, Bangalore 560012, India; [b]Center for Computational Biology, Flatiron Institute, New York, NY 10010; [c]Kavli Institute for Theoretical Physics, University of California, Santa Barbara, CA 93106; [d]Physics Department, University of California, Santa Barbara, CA 93106; [e]Martin A. Fisher School of Physics, Brandeis University, Waltham, MA 02454; [f]Brown Theoretical Physics Center and Department of Physics, Brown University, Providence, RI 02912; [g]Center for Fluid Mechanics and School of Engineering, Brown University, Providence, RI 02912; [h]Biomolecular Science & Engineering Department, University of California, Santa Barbara, CA 93106; and [i]Centre for Biosystems Science and Engineering, Indian Institute of Science, Bangalore 560012, India

1. U. Seifert, Configurations of fluid membranes and vesicles. *Adv. Phys.* **46**, 13–137 (1997).
2. Z. A. Almsherqi, S. D. Kohlwein, Y. Deng, Cubic membranes: A legend beyond the Flatland* of cell membrane organization. *J. Cell Biol.* **173**, 839–844 (2006).
3. X. Michalet, D. Bensimon, Observation of stable shapes and conformal diffusion in genus 2 vesicles. *Science* **269**, 666–668 (1995).
4. W. Longley, T. J. McIntosh, A bicontinuous tetrahedral structure in a liquid-crystalline lipid. *Nature* **303**, 612–614 (1983).
5. H. T. McMahon, J. L. Gallop, Membrane curvature and mechanisms of dynamic cell membrane remodelling. *Nature* **438**, 590–596 (2005).
6. L. V. Chernomordik, M. M. Kozlov, Mechanics of membrane fusion. *Nat. Struct. Mol. Biol.* **15**, 675–683 (2008).
7. E. L. Snapp *et al.*, Formation of stacked ER cisternae by low affinity protein interactions. *J. Cell Biol.* **163**, 257–269 (2003).
8. Y. Bussi *et al.*, Fundamental helical geometry consolidates the plant photosynthetic membrane. *Proc. Natl. Acad. Sci. U.S.A.* **116**, 22366–22375 (2019).
9. S. C. Harrison, Viral membrane fusion. *Nat. Struct. Mol. Biol.* **15**, 690–698 (2008).
10. J. Zimmerberg, M. M. Kozlov, How proteins produce cellular membrane curvature. *Nat. Rev. Mol. Cell Biol.* **7**, 9–19 (2006).
11. Y. S. Bykov *et al.*, The structure of the COPI coat determined within the cell. *eLife* **6**, e32493 (2017).
12. M. Lewicka, L. Mahadevan, Geometry, analysis and morphogenesis: Problems and prospects. *Bull. Am. Math. Soc.* **59**, 331–369 (2022).
13. T. Savin *et al.*, On the growth and form of the gut. *Nature* **476**, 57–62 (2011).
14. W. M. van Rees, E. Vouga, L. Mahadevan, Growth patterns for shape-shifting elastic bilayers. *Proc. Natl. Acad. Sci. U.S.A.* **114**, 11597–11602 (2017).
15. N. P. Mitchell *et al.*, Visceral organ morphogenesis via calcium-patterned muscle contractions. *eLife* **11**, e77355 (2022).
16. E. Karzbrun *et al.*, Human neural tube morphogenesis in vitro by geometric constraints. *Nature* **599**, 268–272 (2021).
17. R. J. Metzger, O. D. Klein, G. R. Martin, M. A. Krasnow, The branching programme of mouse lung development. *Nature* **453**, 745–750 (2008).
18. E. Cerda, L. Mahadevan, Geometry and physics of wrinkling. *Phys. Rev. Lett.* **90**, 074302 (2003).
19. J. Kim, J. A. Hanna, M. Byun, C. D. Santangelo, R. C. Hayward, Designing responsive buckled surfaces by halftone gel lithography. *Science* **335**, 1201–1205 (2012).
20. Y. Klein, E. Efrati, E. Sharon, Shaping of elastic sheets by prescription of non-Euclidean metrics. *Science* **315**, 1116–1120 (2007).
21. J. Huang *et al.*, Capillary wrinkling of floating thin polymer films. *Science* **317**, 650–653 (2007).
22. E. Barry, Z. Dogic, Entropy driven self-assembly of nonamphiphilic colloidal membranes. *Proc. Natl. Acad. Sci. U.S.A.* **107**, 10348–10353 (2010).
23. Y. Yang, E. Barry, Z. Dogic, M. F. Hagan, Self-assembly of 2D membranes from mixtures of hard rods and depleting polymers. *Soft Matter* **8**, 707–714 (2012).
24. A. J. Balchunas *et al.*, Equation of state of colloidal membranes. *Soft Matter* **15**, 6791–6802 (2019).
25. S. Asakura, F. Oosawa, On interaction between two bodies immersed in a solution of macromolecules. *J. Chem. Phys.* **22**, 1255–1256 (1954).
26. W. Helfrich, Elastic properties of lipid bilayers: Theory and possible experiments. *Z. Naturforsch. C* **28**, 693–703 (1973).
27. T. Gibaud *et al.*, Achiral symmetry breaking and positive Gaussian modulus lead to scalloped colloidal membranes. *Proc. Natl. Acad. Sci. U.S.A.* **114**, E3376–E3384 (2017).
28. L. L. Jia, M. J. Zakhary, Z. Dogic, R. A. Pelcovits, T. R. Powers, Chiral edge fluctuations of colloidal membranes. *Phys. Rev. E* **95**, 060701 (2017).
29. T. Gibaud *et al.*, Reconfigurable self-assembly through chiral control of interfacial tension. *Nature* **481**, 348–351 (2012).
30. E. Barry, Z. Dogic, R. B. Meyer, R. A. Pelcovits, R. Oldenbourg, Direct measurement of the twist penetration length in a single smectic A layer of colloidal virus particles. *J. Phys. Chem. B* **113**, 3910–3913 (2009).
31. P. Sharma, A. Ward, T. Gibaud, M. F. Hagan, Z. Dogic, Hierarchical organization of chiral rafts in colloidal membranes. *Nature* **513**, 77–80 (2014).
32. J. M. Miller *et al.*, Conformational switching of chiral colloidal rafts regulates raft-raft attractions and repulsions. *Proc. Natl. Acad. Sci. U.S.A.* **116**, 15792–15801 (2019).
33. J. M. Miller *et al.*, All twist and no bend makes raft edges splay: Spontaneous curvature of domain edges in colloidal membranes. *Sci. Adv.* **6**, eaba2331 (2020).
34. Z. Dogic, S. Fraden, Development of model colloidal liquid crystals and the kinetics of the isotropic–smectic transition. *Philos. Trans. R. Soc. Lond. A* **359**, 997–1015 (2001).
35. E. Grelet, S. Fraden, What is the origin of chirality in the cholesteric phase of virus suspensions? *Phys. Rev. Lett.* **90**, 198302 (2003).
36. E. Barry, D. Beller, Z. Dogic, A model liquid crystalline system based on rodlike viruses with variable chirality and persistence length. *Soft Matter* **5**, 2563–2570 (2009).
37. M. Siavashpouri, P. Sharma, J. Fung, M. F. Hagan, Z. Dogic, Structure, dynamics and phase behavior of short rod inclusions dissolved in a colloidal membrane. *Soft Matter* **15**, 7033–7042 (2019).
38. Z. Dogic, Surface freezing and a two-step pathway of the isotropic-smectic phase transition in colloidal rods. *Phys. Rev. Lett.* **91**, 165701 (2003).
39. L. Kang, T. C. Lubensky, Chiral twist drives raft formation and organization in membranes composed of rod-like particles. *Proc. Natl. Acad. Sci. U.S.A.* **114**, E19–E27 (2017).
40. A. T. Fomenko, A. A. Tuzhilin, *Elements of the Geometry and Topology of Minimal Surfaces in Three-Dimensional Space* (American Mathematical Society, Providence, RI, 1991).
41. P. B. Canham, The minimum energy of bending as a possible explanation of the biconcave shape of the human red blood cell. *J. Theor. Biol.* **26**, 61–81 (1970).
42. A. Balchunas *et al.*, Force-induced formation of twisted chiral ribbons. *Phys. Rev. Lett.* **125**, 018002 (2020).
43. M. Kléman, *Points, Lines, and Walls* (John Wiley & Sons, Chichester, United Kingdom, 1983).
44. M. J. Zakhary *et al.*, Imprintable membranes from incomplete chiral coalescence. *Nat. Commun.* **5**, 3063 (2014).
45. S. A. Akram, A. Behera, P. Sharma, A. Sain, Chiral molecules on curved colloidal membranes. *Soft Matter* **16**, 10310–10319 (2020).
46. C. B. Stanley, H. H. Strey, Measuring osmotic pressure of poly(ethylene glycol) solutions by sedimentation equilibrium ultracentrifugation. *Macromolecules* **36**, 6888–6893 (2003).
47. W. Harbich, R. Servuss, W. Helfrich, Passages in lecithin-water systems. *Z. Naturforsch. C* **33a**, 1013–1017 (1978).
48. W. Helfrich, *Physics of Defects (Les Houches, Session XXXV, 1980)*, R. Balian, M. Kléman, J. P. Poirier, Eds. (North Holland, Amsterdam, the Netherlands, 1981), p. 715.
49. M. M. Terzi, M. F. Ergüder, M. Deserno, A consistent quadratic curvature-tilt theory for fluid lipid membranes. *J. Chem. Phys.* **151**, 164108 (2019).
50. L. Johannes, C. Wunder, P. Bassereau, Bending "on the rocks"–a cocktail of biophysical modules to build endocytic pathways. *Cold Spring Harb. Perspect. Biol.* **6**, a016741 (2014).
51. H. T. McMahon, E. Boucrot, Molecular mechanism and physiological functions of clathrin-mediated endocytosis. *Nat. Rev. Mol. Cell Biol.* **12**, 517–533 (2011).
52. T. C. Südhof, J. Rizo, Synaptic vesicle exocytosis. *Cold Spring Harb. Perspect. Biol.* **3**, a005637 (2011).
53. B. Westermann, Mitochondrial fusion and fission in cell life and death. *Nat. Rev. Mol. Cell Biol.* **11**, 872–884 (2010).
54. P. Rangamani *et al.*, Signaling network triggers and membrane physical properties control the actin cytoskeleton-driven isotropic phase of cell spreading. *Biophys. J.* **100**, 845–857 (2011).
55. B. Pontes *et al.*, Membrane elastic properties and cell function. *PLoS One* **8**, e67708 (2013).
56. M. Hu, J. J. Briguglio, M. Deserno, Determining the Gaussian curvature modulus of lipid membranes in simulations. *Biophys. J.* **102**, 1403–1410 (2012).
57. D. P. Siegel, M. M. Kozlov, The gaussian curvature elastic modulus of N-monomethylated dioleoylphosphatidylethanolamine: Relevance to membrane fusion and lipid phase behavior. *Biophys. J.* **87**, 366–374 (2004).
58. P. Fonda, S. C. Al-Izzi, L. Giomi, M. S. Turner, Measuring Gaussian rigidity using curved substrates. *Phys. Rev. Lett.* **125**, 188002 (2020).

59. T. Baumgart, S. Das, W. W. Webb, J. T. Jenkins, Membrane elasticity in giant vesicles with fluid phase coexistence. *Biophys. J.* **89**, 1067–1080 (2005).
60. S. Semrau, T. Idema, L. Holtzer, T. Schmidt, C. Storm, Accurate determination of elastic parameters for multicomponent membranes. *Phys. Rev. Lett.* **100**, 088101 (2008).
61. P. N. Pusey, W. van Megen, Phase behaviour of concentrated suspensions of nearly hard colloidal spheres. *Nature* **320**, 340–342 (1986).
62. A. van Blaaderen, P. Wiltzius, Real-space structure of colloidal hard-sphere glasses. *Science* **270**, 1177–1179 (1995).
63. P. Schall, I. Cohen, D. A. Weitz, F. Spaepen, Visualizing dislocation nucleation by indenting colloidal crystals. *Nature* **440**, 319–323 (2006).
64. M. He *et al.*, Colloidal diamond. *Nature* **585**, 524–529 (2020).
65. D. Demurtas *et al.*, Direct visualization of dispersed lipid bicontinuous cubic phases by cryo-electron tomography. *Nat. Commun.* **6**, 8915 (2015).
66. H. M. G. Barriga, M. N. Holme, M. M. Stevens, Cubosomes: The next generation of smart lipid nanoparticles? *Angew. Chem. Int. Ed. Engl.* **58**, 2958–2978 (2019).
67. D. Gazeau, A. M. Bellocq, D. Roux, T. Zemb, Experimental evidence for random surface structures in dilute surfactant solutions. *Europhys. Lett.* **9**, 447–452 (1989).
68. M. E. Cates, D. Roux, D. Andelman, S. T. Milner, S. A. Safran, Random surface model for the I_3-phase of dilute surfactant solutions. *Europhys. Lett.* **5**, 733–739 (1988).
69. N. C. Keim, P. Møller, W. W. Zhang, S. R. Nagel, Breakup of air bubbles in water: Memory and breakdown of cylindrical symmetry. *Phys. Rev. Lett.* **97**, 144503 (2006).
70. L. Xiong *et al.*, Flower-like patterns in multi-species bacterial colonies. *eLife* **9**, e48885 (2020).
71. J. Huang, B. Davidovitch, C. D. Santangelo, T. P. Russell, N. Menon, Smooth cascade of wrinkles at the edge of a floating elastic film. *Phys. Rev. Lett.* **105**, 038302 (2010).
72. J. Sambrook, E. F. Fritsch, T. Maniatis, *Molecular Cloning: A Laboratory Manual* (Cold Spring Harbor Laboratory Press, 1989).